ESTIMATING FLUID TERM AND ANISOTROPIC PARAMETERS IN SATURATED TRANSVERSELY ISOTROPIC MEDIA WITH ALIGNED FRACTURES

XINPENG PAN[1,2], GUANGZHI ZHANG[2], JIANXIN LIU[1] and ZHENGYONG REN[1*]

[1] *School of Geoscience and Info-Physics, Central South University, Changsha 410082, P.R. China. renzhengyong@csu.edu.cn*
[2] *School of Sciences, China University of Petroleum (East China), Qingdao 266580, P.R. China.*

(Received June 2, 2019; revised version accepted September 8, 2020)

ABSTRACT

Pan, X.P., Zhang, G.Z., Liu, J.X. and Ren, Z.Y., 2020. Estimating fluid term and anisotropic parameters in saturated transversely isotropic media with aligned fractures. *Journal of Seismic Exploration*, 30: 65-84.

The Gassmann's equation and general linear-slip model can be combined to characterize the effective elastic properties of a fluid-saturated transversely isotropic medium with aligned fractures. Such a medium represents a saturated fractured porous rock with orthorhombic symmetry. Combining the analysis of orthorhombic anisotropic poroelasticity, we first propose the derivation for the weak-anisotropy stiffnesses of a saturated fractured porous medium with orthorhombic symmetry in terms of the moduli of the background homogeneous isotropic rock, Thomsen-type anisotropy parameters, fracture weaknesses, and fluid modulus. Compared with the exact stiffness components, the approximated components of saturated fractured porous media with orthorhombic symmetry satisfy the actual demands in practical use. Using the approximately linearized expressions of the stiffness components of saturated orthorhombic model with the assumption of small Thomsen-type anisotropic parameters and small fracture parameters, we then derive a linearized PP-wave reflection coefficient in such an orthorhombic model, including a fluid term, a rigidity term, a density term, two Thomsen-type anisotropy terms, and three fracture-weakness terms. With a novel parameterization for Thomsen-type anisotropy parameters and fracture weaknesses, we derive an azimuthal elastic impedance equation with decoupled fluid term and anisotropic parameters. Synthetic and real data sets are used to illustrate the proposed approach in fluid saturated fractured porous rocks with orthorhombic symmetry, Sichuan Basin, China.

KEY WORDS: orthorhombic symmetry, fracture weakness, Bayesian seismic inversion, saturated fractured porous media, decoupled fluid and fracture properties.

0963-0651/21/$5.00 © 2021 Geophysical Press Ltd.

INTRODUCTION

A fractured model with orthorhombic symmetry can be formed from a transversely isotropic (VTI) layer with a vertical axis of symmetry containing a single set of vertical, aligned fractures (as illustrated by Fig. 1a, see Tsvankin, 1997; Schoenberg and Helbig, 1997; Bakulin et al., 2000a; Bachrach, 2015; Pan et al., 2017a, 2017b). Moreover, an isotropic or VTI layer containing two orthorhombic sets of vertical fractures with rotationally invariant properties also exhibits orthorhombic anisotropy (as illustrated by Figs. 1b and 1c, see Bakulin et al., 2000a; 2002; Downton and Roure, 2015; Chen et al., 2017; Pan et al., 2018a). A more complicated but should not be ignored fractured model is monoclinic symmetry, which can be formed by an isotropic or VTI layer containing two or more non-orthogonal sets of vertical fracture with rotationally invariant properties (Sayers, 1998; Bakulin et al., 2000b). However, this paper focuses on the fractured models with orthorhombic symmetry to perform the seismic fracture characterization and fluid discrimination.

Discriminations of fluid and fracture properties are the keys to the exploration and production in hydrocarbon reservoirs, and the 'sweet spots' information of high fracture density properties is required to target locations for infill drilling and maximize production (Sayers, 2009; Far et al., 2013; Zong and Yin, 2016). For the subsurface fracture detection, azimuthal seismic reflection amplitudes are widely used to estimate the fracture properties (Bachrach et al., 2009; Liu and Martinez, 2012; Pan et al., 2018b). Estimation of the fluid indicators from the prestack seismic data has been widely used in fluid identification (Russell et al., 2011). For the case of fracture-induced anisotropy, the fracture properties are usually characterized by the fracture compliances or weaknesses, in which the normal compliance Z_N or weakness δ_N exhibits significant dependence on fluid infills, whereas the tangential compliance Z_T or weakness δ_T do not vary with the fluid contents (Schoenberg and Douma, 1988). Therefore, the compliance ratio Z_N/Z_T is treated as a fluid indicator in fractures, and Shaw and Sen (2006) use the corresponding weakness ratio δ_N/δ_T as a fluid indicator. However, these fracture fluid indicators (FFI) mentioned above present a coupling effect of fracture density and fluid infills, resulting in uncertainties of fluid and fracture characterization in fractured porous media with transversely isotropic symmetry (Pan et al., 2018c, 2018d). Therefore, we decouple the combined effects of fracture and fluid properties on seismic characterization in a saturated transversely isotropic media with aligned fractures.

For fractured porous rocks, the anisotropic Gassmann's (1951) equations and linear-slip model can be combined to describe the fluid property in fractures (Gurevich, 2003; Huang et al., 2015). Considering two layers with the interface between them, we derive the linearized approximations of stiffnesses in an orthorhombic anisotropic medium. Using a first-order perturbation for elastic and anisotropic parameters (Thomsen, 1986; Pšenčík and Vavryčuk, 1998; Golikov and Stovas, 2010; Ivanov and Stovas, 2017), we derive the PP-wave reflection coefficient in such a

fluid-saturated fractured porous media with orthorhombic symmetry, including a fluid term, a rigidity term, a density term, two Thomsen's anisotropy terms, and three weakness terms. With a novel parameterization for anisotropic characteristic parameters with orthorhombic symmetry, we derive an azimuthal elastic impedance (AEI) equation for decoupled fluid term and fracture weakness parameters. We implement the Bayesian AEI iterative inversion to perform the seismic fluid identification and fracture characterization. The inversion results demonstrate that the fluid term and fracture weakness parameters can be reliably inverted in such a fractured porous medium with orthorhombic symmetry.

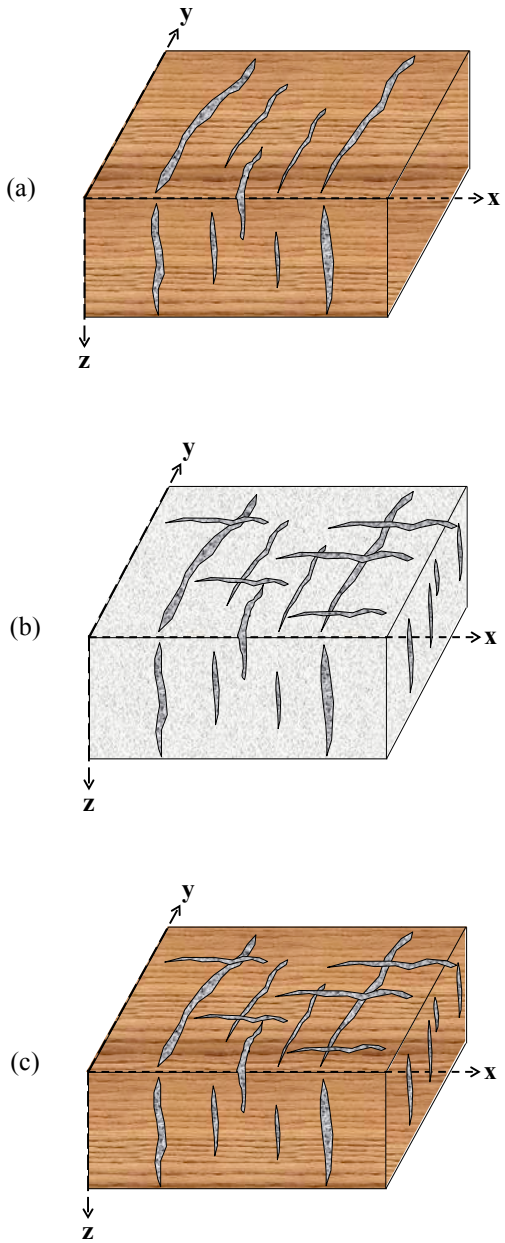

Fig. 1. Schematic diagram of fractured models with orthorhombic symmetry, where (a) is formed by a single set of vertical fractures embedded in a VTI background, (b) is formed by two orthogonal sets of rotationally invariant vertical fracture embedded in an isotropic background, and (c) is formed by two orthogonal sets of rotationally invariant vertical fracture embedded in a VTI background.

THEORY and METHOD

Effective elastic properties and PP-wave reflection coefficient of fractured porous media with orthorhombic symmetry

Horizontal fine layers permeated with aligned vertical fractures are an equivalent orthorhombic anisotropic medium (Schoenberg and Helbig, 1997). If the background porous rock with VTI symmetry contains one set of aligned fractures, we combine the weak-anisotropy approximations of Thomsen's (1986) anisotropic parameters (Tsvankin, 1997; Pan et al., 2018a), and give the expressions for dry-rock weak-anisotropy approximate stiffnesses in an orthorhombic medium as (Schoenberg and Helbig, 1997)

$$C_{11}^{ORT-dry} = M_{dry}\left(1-\delta_N^{dry}\right)+2M_{dry}\varepsilon_b, \tag{1a}$$

$$C_{12}^{ORT-dry} = \lambda_{dry}\left(1-\delta_N^{dry}\right)+2M_{dry}\varepsilon_b-4\mu\gamma_b, \tag{1b}$$

$$C_{13}^{ORT-dry} = \lambda_{dry}\left(1-\delta_N^{dry}\right)+M_{dry}\delta_b, \tag{1c}$$

$$C_{22}^{ORT-dry} = M_{dry}\left(1-\chi^2\delta_N^{dry}\right)+2M_{dry}\varepsilon_b, \tag{1d}$$

$$C_{23}^{ORT-dry} = \lambda_{dry}\left(1-\chi\delta_N^{dry}\right)+M_{dry}\delta_b, \tag{1e}$$

$$C_{33}^{ORT-dry} = M_{dry}\left(1-\chi^2\delta_N^{dry}\right), \tag{1f}$$

$$C_{44}^{ORT-dry} = \mu, \tag{1g}$$

$$C_{55}^{ORT-dry} = \mu\left(1-\delta_V\right), \tag{1h}$$

and

$$C_{66}^{ORT-dry} = \mu\left(1-\delta_H\right)-2\mu\gamma_b. \tag{1i}$$

Here M_{dry} and μ are the compressional (P-wave) modulus and shear (S-wave) moduli of dry rocks, respectively; $\lambda_{dry}=M_{dry}-2\mu$ represents the first Lamé parameter of dry rocks, and $\chi=\lambda_{dry}/M_{dry}$; δ_N, δ_V, and δ_H denote the so-called dimensionless normal, vertically and horizontally shear fracture weaknesses in different directions due to the presence of fractures, respectively; ε_b, γ_b, δ_b represent the Thomsen-type anisotropic parameters of VTI background (Sayers, 1994).

According to Gurevich (2003) and Pan et al. (2018c, 2018d), the fluid saturated stiffnesses of fractured porous media with orthorhombic symmetry can be finally expressed in this form

$$C_{mn}^{ORT-sat} = C_{mn}^{ORT-dry} + \frac{\left(1-\dfrac{\sum_{m=1}^{3} C_{mn}^{ORT-dry}}{3K_0}\right)\left(1-\dfrac{\sum_{n=1}^{3} C_{mn}^{ORT-dry}}{3K_0}\right)}{\dfrac{1}{K_0}-\dfrac{\sum_{m=1}^{3}\sum_{n=1}^{3} C_{mn}^{ORT-dry}}{9K_0^2}-\dfrac{\phi}{K_0}\left(1-\dfrac{K_0}{K_f}\right)}, \qquad m,n=1,2,\mathrm{K}\ ,6 \tag{2}$$

where $C_{mn}^{ORT-dry}$ and $C_{mn}^{ORT-sat}$ denote the gas-saturated (or dry) and fluid-saturated stiffnesses with orthorhombic anisotropy; ϕ denotes the porosity of rocks, which is the sum of the matrix porosity ϕ_b and the fracture porosity ϕ_f; K_0 denotes the mineral modulus, and K_f denotes the fluid modulus.

Based on the linearized dry-rock weak-anisotropy approximations of stiffnesses, we derive the saturated stiffnesses $\boldsymbol{C}_{ij}^{ORT-sat}$ with orthorhombic symmetry, which are given by

$$\begin{aligned} C_{11}^{ORT-sat} \approx{}& M_{dry}\left(1-\delta_N^{dry}\right)+2M_{dry}\varepsilon_b+\frac{\left(1-K_{dry}/K_0\right)^2}{\phi}K_f+2\frac{\left(K_{dry}/K_0\right)\left(1-K_{dry}/K_0\right)}{\phi}K_f\delta_N^{dry} \\ &-2\frac{\left(K_{dry}/K_0\right)\left(1-K_{dry}/K_0\right)}{\phi}K_f\frac{4M_{dry}\varepsilon_b-4\mu\gamma_b+M_{dry}\delta_b}{3K_{dry}}, \end{aligned} \tag{3a}$$

$$\begin{aligned} C_{12}^{ORT-sat} \approx{}& \lambda_{dry}\left(1-\delta_N^{dry}\right)+2M_{dry}\varepsilon_b-4\mu\gamma_b+\frac{\left(1-K_{dry}/K_0\right)^2}{\phi}K_f+\frac{\left(K_{dry}/K_0\right)\left(1-K_{dry}/K_0\right)}{\phi}K_f\left(1+\chi\right)\delta_N^{dry} \\ &-2\frac{\left(K_{dry}/K_0\right)\left(1-K_{dry}/K_0\right)}{\phi}K_f\frac{4M_{dry}\varepsilon_b-4\mu\gamma_b+M_{dry}\delta_b}{3K_{dry}}, \end{aligned} \tag{3b}$$

$$\begin{aligned} C_{13}^{ORT-sat} \approx{}& \lambda_{dry}\left(1-\delta_N^{dry}\right)+M_{dry}\delta_b+\frac{\left(1-K_{dry}/K_0\right)^2}{\phi}K_f+\frac{\left(K_{dry}/K_0\right)\left(1-K_{dry}/K_0\right)}{\phi}K_f\left(1+\chi\right)\delta_N^{dry} \\ &-\frac{\left(K_{dry}/K_0\right)\left(1-K_{dry}/K_0\right)}{\phi}K_f\frac{4M_{dry}\varepsilon_b-4\mu\gamma_b+3M_{dry}\delta_b}{3K_{dry}}, \end{aligned} \tag{3c}$$

$$\begin{aligned} C_{22}^{ORT-sat} \approx{}& M_{dry}\left(1-\chi^2\delta_N^{dry}\right)+2M_{dry}\varepsilon_b+\frac{\left(1-K_{dry}/K_0\right)^2}{\phi}K_f+2\frac{\left(K_{dry}/K_0\right)\left(1-K_{dry}/K_0\right)}{\phi}K_f\chi\delta_N^{dry} \\ &-2\frac{\left(K_{dry}/K_0\right)\left(1-K_{dry}/K_0\right)}{\phi}K_f\frac{4M_{dry}\varepsilon_b-4\mu\gamma_b+M_{dry}\delta_b}{3K_{dry}}, \end{aligned} \tag{3d}$$

$$\begin{aligned} C_{23}^{ORT-sat} \approx{}& \lambda_{dry}\left(1-\chi\delta_N^{dry}\right)+M_{dry}\delta_b+\frac{\left(1-K_{dry}/K_0\right)^2}{\phi}K_f+2\frac{\left(K_{dry}/K_0\right)\left(1-K_{dry}/K_0\right)}{\phi}K_f\chi\delta_N^{dry} \\ &-\frac{\left(K_{dry}/K_0\right)\left(1-K_{dry}/K_0\right)}{\phi}K_f\frac{4M_{dry}\varepsilon_b-4\mu\gamma_b+3M_{dry}\delta_b}{3K_{dry}}, \end{aligned} \tag{3e}$$

$$C_{33}^{ORT-sat} \approx M_{dry}\left(1-\chi^2\delta_N^{dry}\right)+\frac{\left(1-K_{dry}/K_0\right)^2}{\phi}K_f+2\frac{\left(K_{dry}/K_0\right)\left(1-K_{dry}/K_0\right)}{\phi}K_f\chi\delta_N^{dry} - 2\frac{\left(K_{dry}/K_0\right)\left(1-K_{dry}/K_0\right)}{\phi}K_f\frac{2M_{dry}\delta_b}{3K_{dry}}, \tag{3f}$$

$$C_{44}^{ORT-sat}=\mu, \tag{3g}$$

$$C_{55}^{ORT-sat}=\mu\left(1-\delta_V\right), \tag{3h}$$

and

$$C_{66}^{ORT-sat}=\mu\left(1-\delta_H\right)-2\mu\gamma_b. \tag{3i}$$

The comparisons between the exact [eq. (2)] and approximate [eqs. (3a)-(3i)] components of stiffness tensor are illustrated in Fig. 2 to demonstrate the accuracy of derived stiffnesses for the fluid-saturated fractured porous medium with orthorhombic symmetry. The fractured porous rock is assumed to be homogeneously saturated with water and gas. From the comparative analysis of Figs. 2a and 2b, we see the differences between the exact and approximate stiffnesses decrease as the gas saturation increases. In addition, we find the differences increase with the decreasing normal weakness illustrated from the Figs. 2b and 2c. Even when the Thomsen-type anisotropic parameters turn into zero, the differences are still small (Figs. 2b and 2d).

Using the assumptions of weak anisotropy, small weak fracture weaknesses, and weak elastic contrast across an interface separating two orthorhombic anisotropic media, the first-order perturbations for saturated stiffnesses with orthorhombic symmetry can be derived. Integrating the perturbations in stiffnesses, the reflection coefficient of an orthorhombic medium can be defined as

$$R_{PP}^{ORT}=\frac{\Delta\rho}{4\rho}\left(\xi\sec^2\theta\right)+\sum_{m=1}^{6}\sum_{n=1}^{6}\frac{\Delta C_{mn}^{ORT-sat}}{4\rho}\left(\eta_{mn}\sec^2\theta\right), \tag{4}$$

where θ denotes the angle of incidence, and the symbol Δ denotes the perturbations in property parameters; ξ and η_{mn} are two parameters related to slowness and polarization vectors, which can be found in Shaw and Sen (2004).

Using the above methods and derived equations, we can derive the linearized PP-wave reflection coefficient with decoupled fluid and fracture parameters in orthorhombic anisotropic media, including a fluid term, a rigidity term, a density term, two Thomsen-type anisotropy terms, and three weakness terms, which is given by

$$R_{PP}(\theta,\varphi)=a_f(\theta)\frac{\Delta f}{f}+a_\mu(\theta)\frac{\Delta\mu}{\mu}+a_\rho(\theta)\frac{\Delta\rho}{\rho}+a_{\varepsilon_b}(\theta)\Delta\varepsilon_b+a_{\delta_b}(\theta)\Delta\delta_b \\ +a_{\delta_N}(\theta,\varphi)\Delta\delta_N^{dry}+a_{\delta_V}(\theta,\varphi)\Delta\delta_V+a_{\delta_H}(\theta,\varphi)\Delta\delta_H, \tag{5}$$

where

$$a_f(\theta)=\left(1-\frac{\gamma_{dry}^2}{\gamma_{sat}^2}\right)\frac{\sec^2\theta}{4},\quad a_\mu(\theta)=\frac{\gamma_{dry}^2}{\gamma_{sat}^2}\frac{\sec^2\theta}{4}-\frac{2}{\gamma_{sat}^2}\sin^2\theta,\quad a_\rho(\theta)=\frac{1}{2}-\frac{\sec^2\theta}{4},$$
$$a_{\varepsilon_b}(\theta)=\frac{\gamma_{dry}^2}{\gamma_{sat}^2}\frac{\sin^2\theta\tan^2\theta}{2},\quad a_{\delta_b}(\theta)=\frac{\gamma_{dry}^2}{\gamma_{sat}^2}\frac{\sin^2\theta}{2},$$
$$a_{\delta_N}(\theta,\varphi)=-\frac{\gamma_{dry}^2}{\gamma_{sat}^2}\frac{\sec^2\theta}{4}\left[\frac{2}{\gamma_{sat}^2}\left(\sin^2\theta\sin^2\varphi+\cos^2\theta\right)-1\right]^2, \tag{6}$$
$$a_{\delta_V}(\theta,\varphi)=\frac{1}{\gamma_{sat}^2}\sin^2\theta\cos^2\varphi,\qquad a_{\delta_H}(\theta,\varphi)=-\frac{1}{\gamma_{sat}^2}\sin^2\theta\tan^2\theta\sin^2\varphi\cos^2\varphi.$$

Here φ is the azimuthal angle, and the subscripts dry and sat denote the dry and saturated quantities;, $\gamma_{dry}^2=M_{dry}/\mu$ and $\gamma_{sat}^2=M_{sat}/\mu$, which can be calculated following Russell et al. (2011).

Azimuthal elastic impedance inversion in orthorhombic anisotropic media

To stably estimate the anisotropic parameters, we propose the new parameterization expressions for anisotropic parameters (Pan et al., 2017a). The proposed Thomsen-type quasi-anisotropy parameters are given by

$$_q\varepsilon_b=\frac{1}{1-\varepsilon_{b0}}\left(\varepsilon_b+1-\varepsilon_{b0}\right), \tag{7a}$$

and

$$_q\delta_b=\frac{1}{1-\delta_{b0}}\left(\delta_b+1-\delta_{b0}\right). \tag{7b}$$

And the proposed fracture quasi-weaknesses are given by

$$_q\delta_N^{dry}=\frac{1}{1-\delta_{N0}^{dry}}\left(\delta_N^{dry}+1-\delta_{N0}^{dry}\right), \tag{8a}$$

$$_q\delta_V=\frac{1}{1-\delta_{V0}}\left(\delta_V+1-\delta_{V0}\right), \tag{8b}$$

and

$$_q\delta_H=\frac{1}{1-\delta_{H0}}\left(\delta_H+1-\delta_{H0}\right). \tag{8c}$$

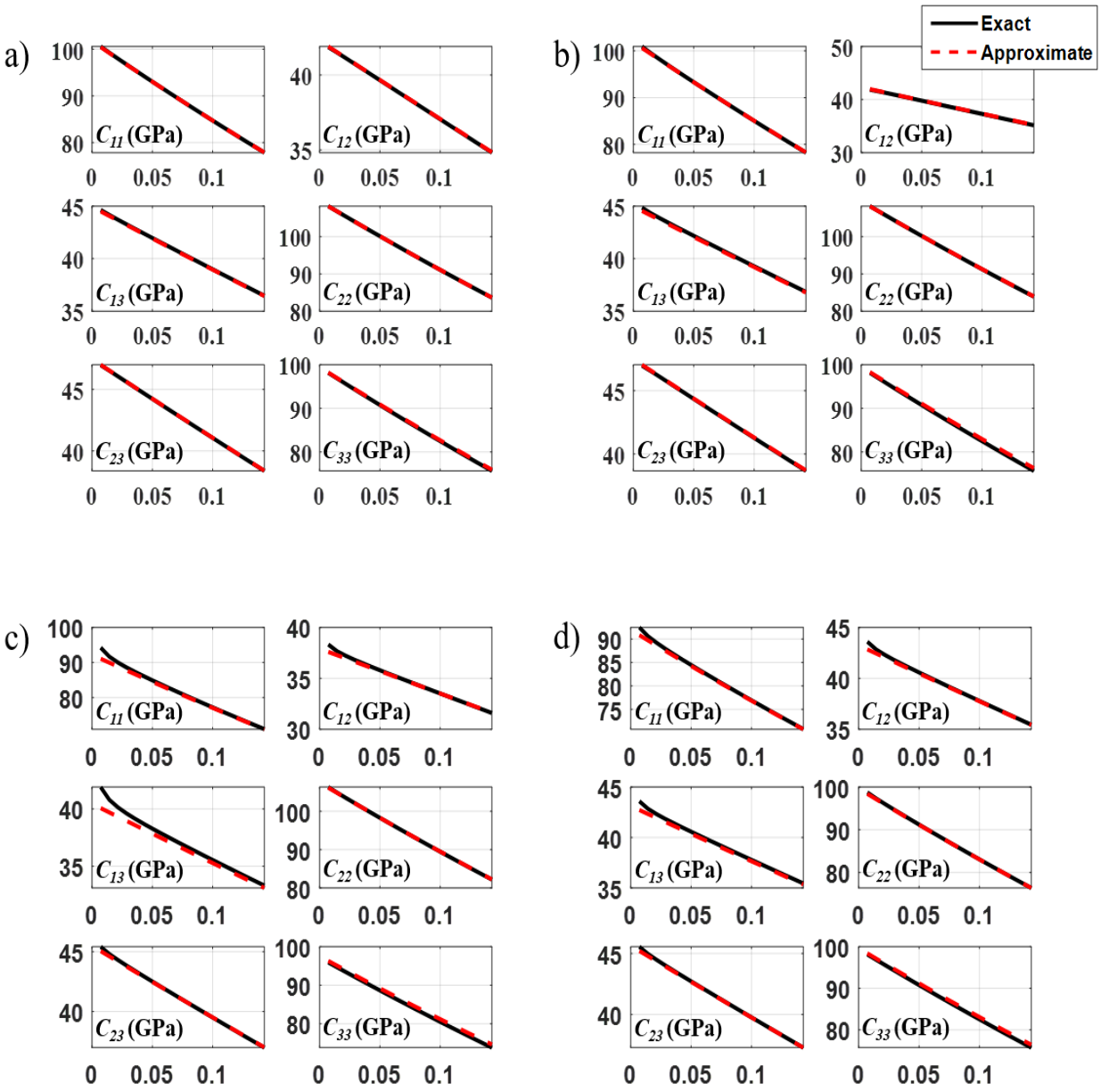

Fig. 2. Comparisons between the exact (black) and approximate (red) components of stiffness tensor for a gas-saturated fractured porous rock with orthorhombic symmetry, where
(a) Gas content percent=30%, δ_N=0.1, ε_b=0.05, δ_b=0.02, γ_b=0.1;
(b) Gas content percent=70%, δ_N=0.1, ε_b=0.05, δ_b=0.02, γ_b=0.1;
(c) Gas content percent=70%, δ_N=0.2, ε_b=0.05, δ_b=0.02, γ_b=0.1; and
(d) Gas content percent=70%, δ_N=0.1, ε_b=0, δ_b=0, γ_b=0.

In the above equations, ε_{b0}, δ_{b0}, δ_{N0}^{dry}, δ_{V0}, and δ_{H0} represent the average quantities of Thomsen-type anisotropic parameters and fracture weaknesses.

According to Connolly (1999) and Martins (2006), the reflection coefficient in orthorhombic anisotropic media can be approximated as

$$\begin{aligned} R_{PP}(\theta,\varphi) &\approx \frac{1}{2}\frac{\Delta EI(\theta,\varphi)}{EI(\theta,\varphi)} \\ &\approx a_f(\theta)\frac{\Delta f}{f} + a_\mu(\theta)\frac{\Delta\mu}{\mu} + a_\rho(\theta)\frac{\Delta\rho}{\rho} + a_{\varepsilon_b}(\theta)\frac{\Delta_q\varepsilon_b}{{}_q\varepsilon_b} + a_{\delta_b}(\theta)\frac{\Delta_q\delta_b}{{}_q\delta_b} \\ &+ a_{\delta_N}(\theta,\varphi)\frac{\Delta\left({}_q\delta_N^{dry}\right)}{{}_q\delta_N^{dry}} + a_{\delta_V}(\theta,\varphi)\frac{\Delta\left({}_q\delta_V\right)}{{}_q\delta_V} + a_{\delta_H}(\theta,\varphi)\frac{\Delta\left({}_q\delta_H\right)}{{}_q\delta_H}, \end{aligned} \quad (9)$$

where *EI* denotes the elastic impedance.

The relative contrasts in eq. (9) can be approximately as

$$\Delta EI/EI \approx \Delta\left[\ln EI\right],\ \ \Delta f/f \approx \Delta\left[\ln f\right],\ \ \Delta\mu/\mu \approx \Delta\left[\ln\mu\right],\ \ \Delta\rho/\rho \approx \Delta\left[\ln\rho\right],$$
$$\Delta\left({}_q\varepsilon_b\right)/{}_q\varepsilon_b \approx \Delta\left[\ln\left({}_q\varepsilon_b\right)\right], \quad \Delta\left({}_q\delta_b\right)/{}_q\delta_b \approx \Delta\left[\ln\left({}_q\delta_b\right)\right],$$
$$\Delta\left({}_q\delta_N^{dry}\right)/{}_q\delta_N^{dry} \approx \Delta\left[\ln\left({}_q\delta_N^{dry}\right)\right],\ \ \Delta\left({}_q\delta_V\right)/{}_q\delta_V \approx \Delta\left[\ln\left({}_q\delta_V\right)\right],$$
$$\text{and}\ \ \Delta\left({}_q\delta_H\right)/{}_q\delta_H \approx \Delta\left[\ln\left({}_q\delta_H\right)\right]. \quad (10)$$

Assuming the continuous variations in EI and model parameters, the relative contrasts in eq. (10) can be substituted by the linear differential expressions:

Following the proposed Bayesian AEI inversion (Pan et al., 2017a), we iteratively solve this inverse problem.

$$\Delta\left[\ln EI\right] \approx d\left[\ln EI\right],\ \ \Delta\left[\ln f\right] \approx d\left[\ln f\right],\ \Delta\left[\ln\mu\right] \approx d\left[\ln\mu\right],\ \Delta\left[\ln\rho\right] \approx d\left[\ln\rho\right],$$
$$\Delta\left[\ln\left({}_q\varepsilon_b\right)\right] \approx d\left[\ln\left({}_q\varepsilon_b\right)\right],\ \ \Delta\left[\ln\left({}_q\delta_b\right)\right] \approx d\left[\ln\left({}_q\delta_b\right)\right],$$
$$\Delta\left[\ln\left({}_q\delta_N^{dry}\right)\right] \approx d\left[\ln\left({}_q\delta_N^{dry}\right)\right], \quad (11)$$
$$\Delta\left[\ln\left({}_q\delta_V\right)\right] \approx d\left[\ln\left({}_q\delta_V\right)\right], \quad \text{and} \quad \Delta\left[\ln\left({}_q\delta_H\right)\right] \approx d\left[\ln\left({}_q\delta_H\right)\right].$$

Finally, the azimuthal elastic impedance (AEI) equation can be written as

$$EI(\theta,\varphi)=[f]^{2a_f(\theta)}\cdot[\mu]^{2a_\mu(\theta)}\cdot[\rho]^{2a_\rho(\theta)}\cdot\left[{}_q\varepsilon_b\right]^{2a_{\varepsilon_b}(\theta)}\cdot\left[{}_q\delta_b\right]^{2a_{\delta_b}(\theta)}\cdot \left[{}_q\delta_N^{dry}\right]^{2a_{\delta_N}(\theta,\varphi)}\cdot\left[{}_q\delta_V\right]^{2a_{\delta_V}(\theta,\varphi)}\cdot\left[{}_q\delta_H\right]^{2a_{\delta_H}(\theta,\varphi)}. \quad (12)$$

EXAMPLES

Synthetic example

A logging data acquired in a saturated fractured porous field is used to demonstrate the proposed Bayesian AEI inversion for decoupled fluid and fracture properties. We first estimate the logging information of Thomsen-type anisotropic parameters and fracture weaknesses using the effective rock-physics model (Pan et al., 2017b). The process of constructing the rock-physics model of a fractured porous medium with orthorhombic symmetry is illustrated in Fig. 3 to be used for estimating the anisotropic well log information. Adding a random Gaussian noise to the noise-free synthetic data produces the noisy data, in which the different signal-to-noise-ratios (SNRs) are 5 (Fig. 4a) and 2 (Fig. 4b), respectively. The six azimuths are 0^0, 30^0, 60^0, 90^0, 120^0, and 150^0. We then implement the Bayesian AEI inversion for decoupled fluid and fracture properties.

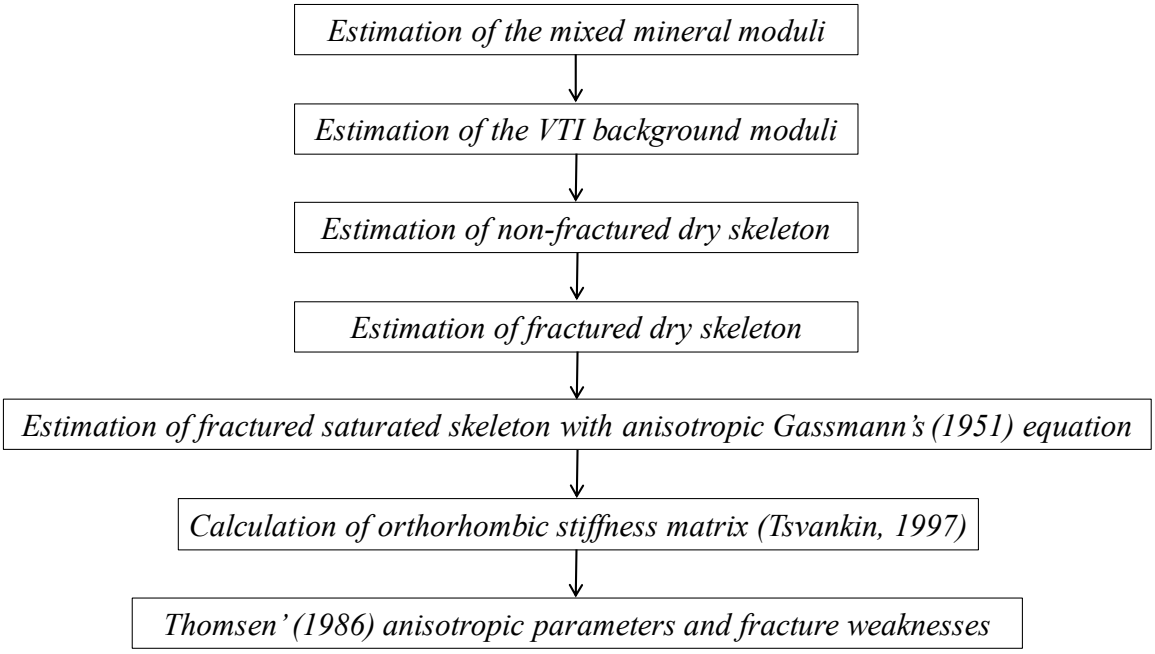

Fig. 3. Process of constructing the rock-physics model with orthorhombic symmetry to estimate the anisotropic well log information.

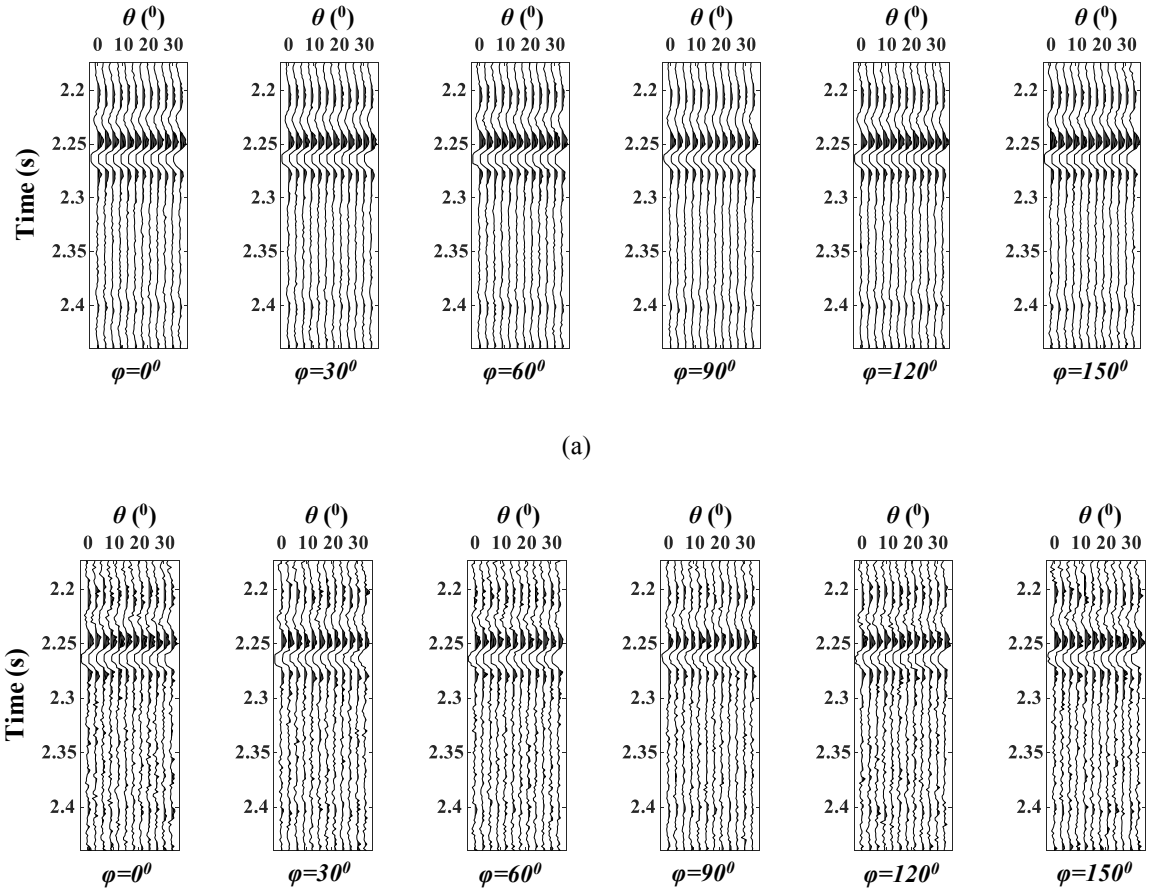

Fig. 4**.** Synthetic seismic angle gathers with different SNRS, where (a) SNR = 5, and (b) SNR = 2.

The original (black), initial (green) and inverted (red) well logs are demonstrated in Fig. 5, respectively. Figs. 5 and 6 are the inversion results with SNRs being 5 and 2, respectively. From the inversion results, we see that the model parameters are reasonably inverted even though the initial models of model parameters are fairly smoothing. Therefore, even in the cases of relatively low SNR, we can still get the reasonable inversion results of model parameters. Figs. 7a and 7b are the seismic data synthesized by inverted model parameters and convolution model. We find that the errors between the original and the synthetic data are small enough to demonstrate the applicability of proposed AEI inversion approach.

Field example

We demonstrate the Bayesian AEI inversion approach using a field data acquired in Sichuan Basin, Southwest China. The target layers mainly contain brine and gas, but belongs to low-porosity and low-permeability reservoir, in which its lithology is principally thick gray dolomite rocks. Moreover, before the inversion, the azimuthal seismic data should be

processed and preconditioned to guarantee that the observable PP-wave reflected amplitudes are the accurate reaction of the response of subsurface interfaces, and the workflow includes wave-front diffusion compensation, noise suppressed in multiple domains, spherical divergence correlation, inverse Q filtering, surface-consistent amplitude correction, pre-stack residual amplitude compensation, deconvolution, COV binning, migration velocity analysis, etc.

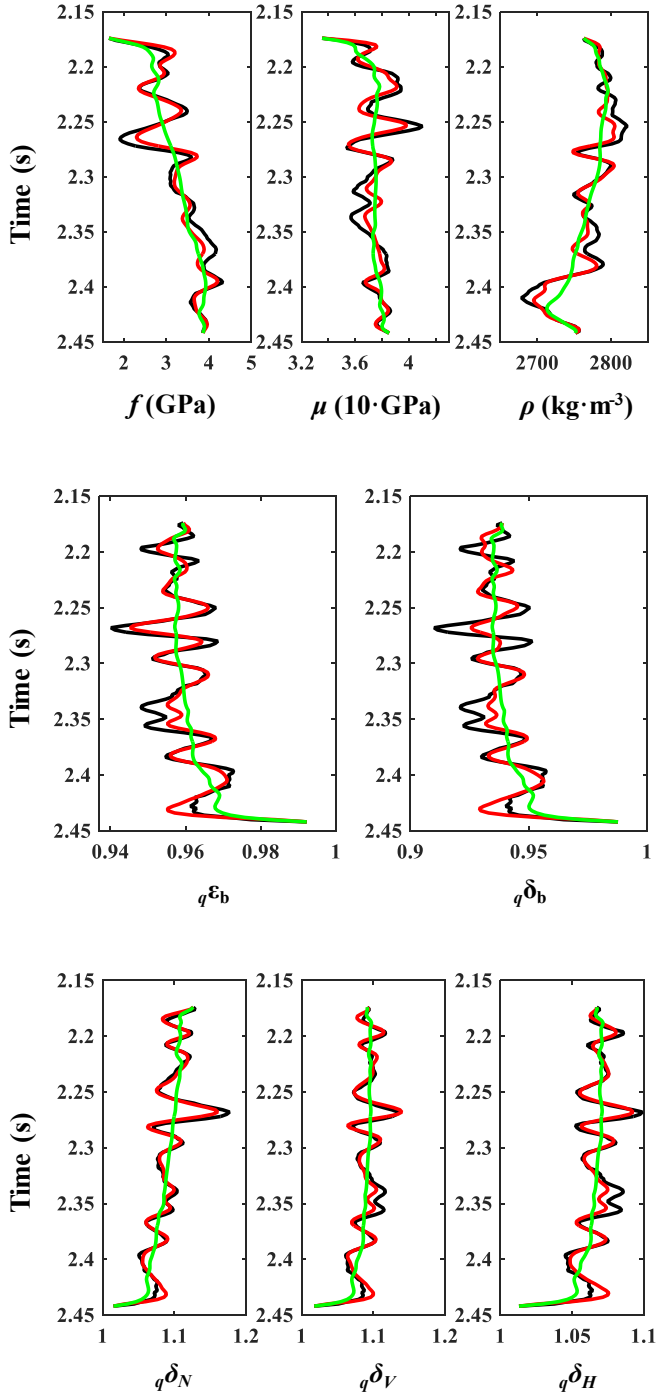

Fig. 5. Estimated model parameters using synthetic angle gathers with SNR = 5, where (a) the fluid term, shear modulus, and density parameters, (b) the Thomsen's quasi-anisotropy parameters, and (c) the fracture quasi-weaknesses.

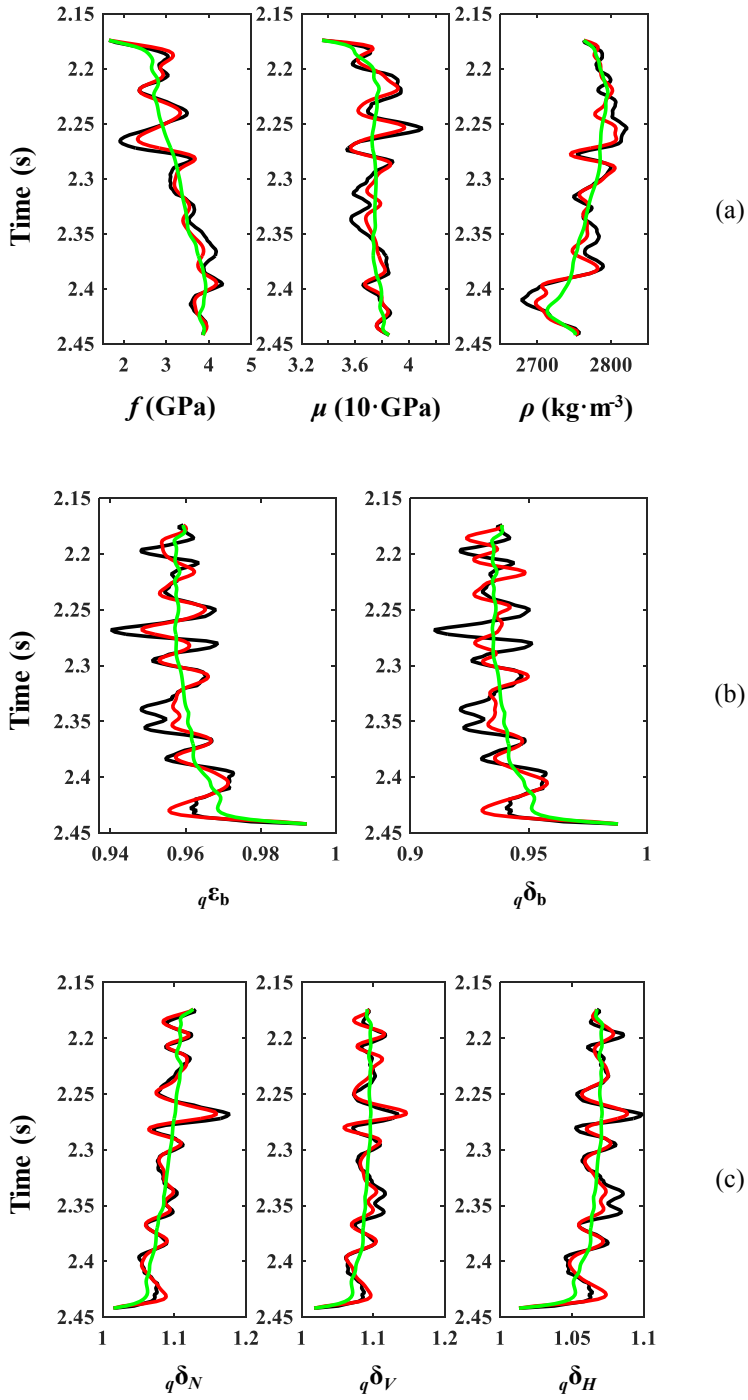

Fig. 6. Estimated model parameters using synthetic angle gathers with SNR = 2, where (a) the fluid term, shear modulus, and density parameters, (b) the Thomsen's quasi-anisotropy parameters, and (c) the fracture quasi-weaknesses.

The input data include four azimuthal seismic data with average angles of azimuth being 22.5^0 (a range between 0^0 and 45^0), 67.5^0 (a range between 45^0 and 90^0), 112.5^0 (a range between 90^0 and 135^0) and 157.5^0 (a range between 135^0 and 180^0), respectively. It needs to be emphasized that the inversion accuracy can be improved by optimization for the strategy of azimuthal sector division. Therefore, the divided each azimuth among the azimuthal data should be ensured to contain enough SNRs, and the number of coverage times in each azimuth should be as uniform as possible.

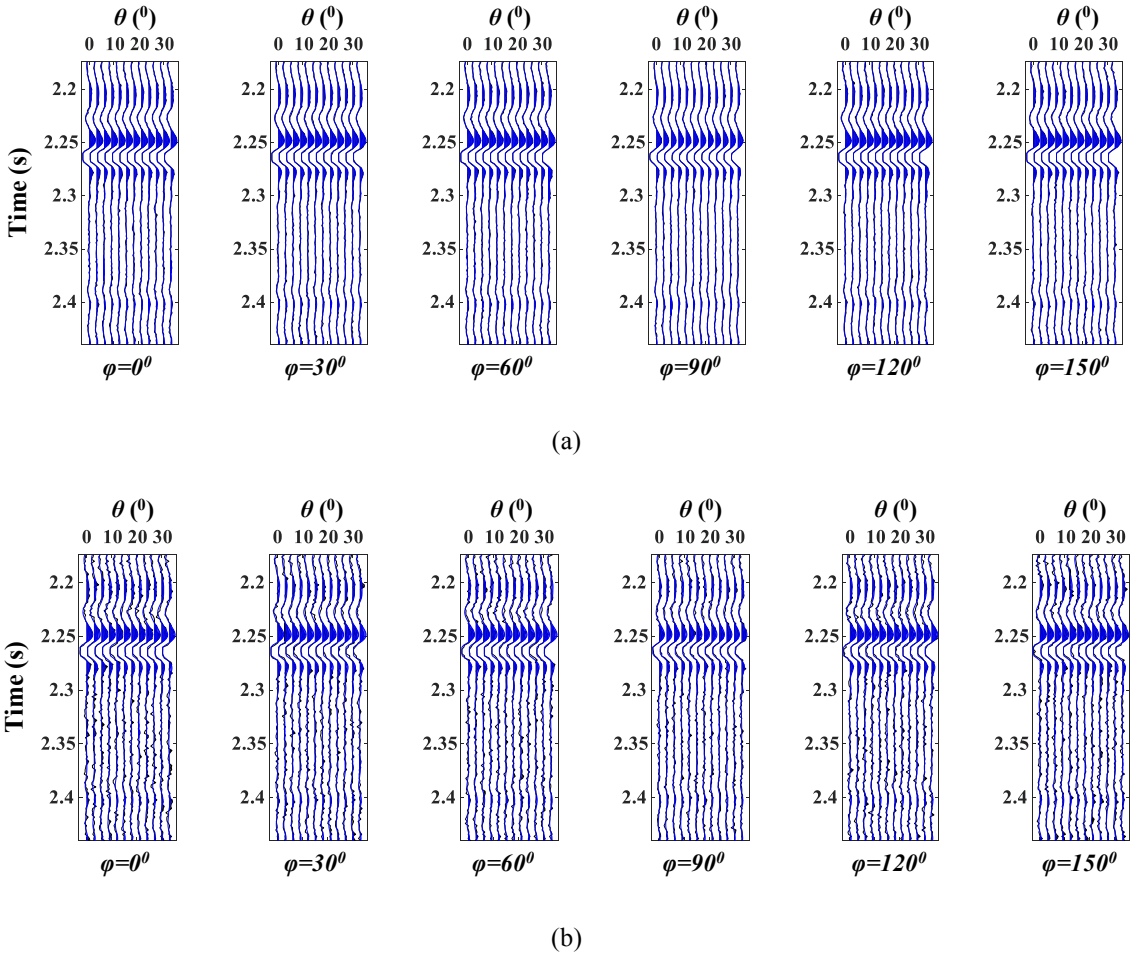

Fig. 7. Comparison between the original and synthetic angle gathers with different SNRS, where (a) SNR = 5, and (b) SNR = 2.

Then the Bayesian AEI inversion are performed by using the azimuthal data. Fig. 8 just shows the input seismic data with the first azimuth, where the average angles of incidence for the near, middle and far angle-stacks are 5^0 (a range between 0^0 and 10^0), 15^0 (a range between 10^0 and 20^0) and 25^0 (a range between 20^0 and 30^0), respectively. The corresponding inverted azimuthal elastic impedance sections are displayed in Fig. 9. We find that three inversion results in different angles of incidence show differences in values, but the low-value anomaly of estimated elastic impedance are related to the gas-bearing layers based on the analysis of well log data. Other azimuthal data can be also processed by using the same processing method, and we won't show them here for brevity.

The inverted model parameters are shown in Figs. 10, 11, and 12. The information of Well A is used to construct the initial model parameters of elastic and fracture parameters, and the white ellipse illustrates the gas-bearing layers. The Well B is used to demonstrate the reliability and stability of inversion results, and we can see that the low-value elastic and background VTI parameters and high-value fracture parameters are more sensitive to the gas-bearing layers, in which the inverted fluid term and fracture weaknesses present a good indicator of hydrocarbon response and

fracture-development zones. As a result, the fluid indicator and fracture weaknesses can be provided as sensitive indicators for gas-bearing fractured reservoirs.

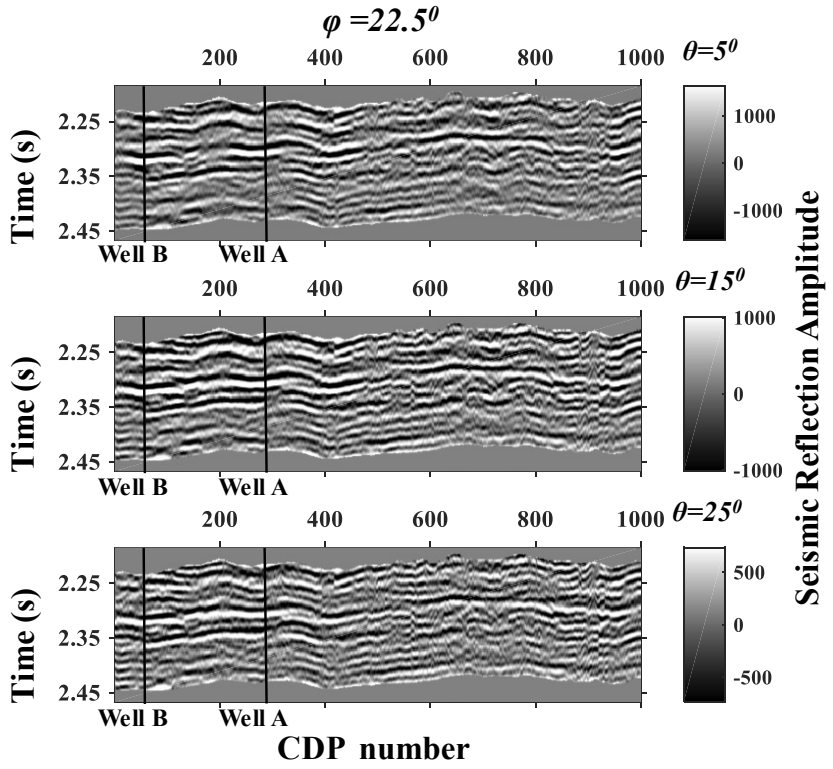

Fig. 8. Input data with the first azimuth.

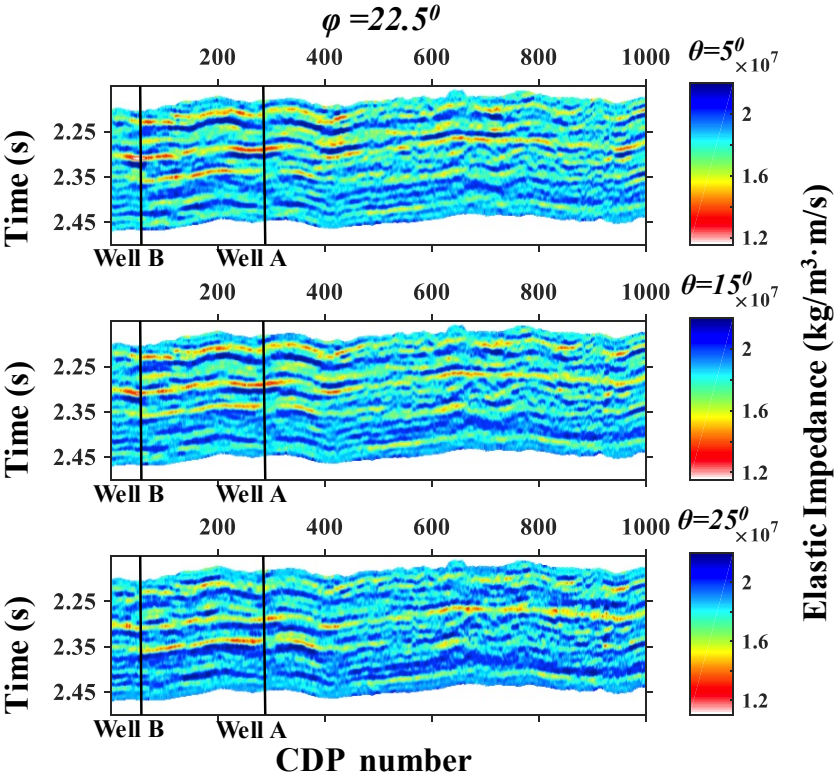

Fig. 9. Output data with the first azimuth.

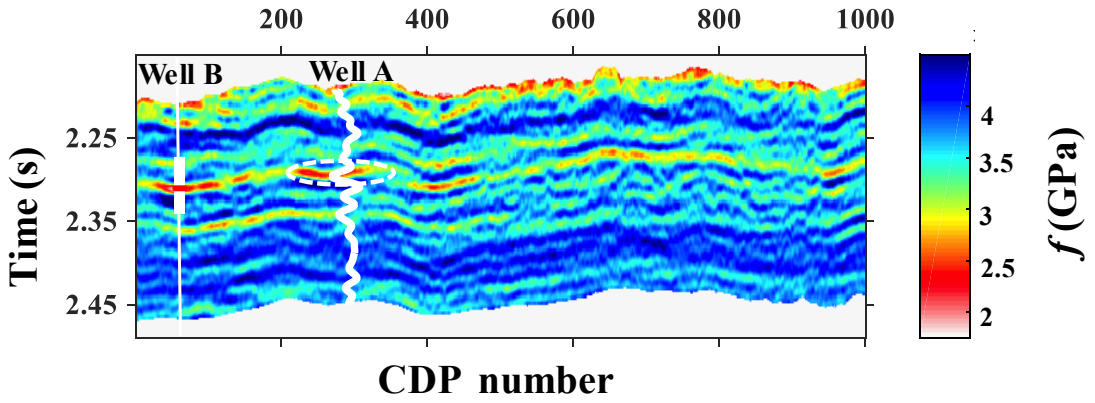

(a)

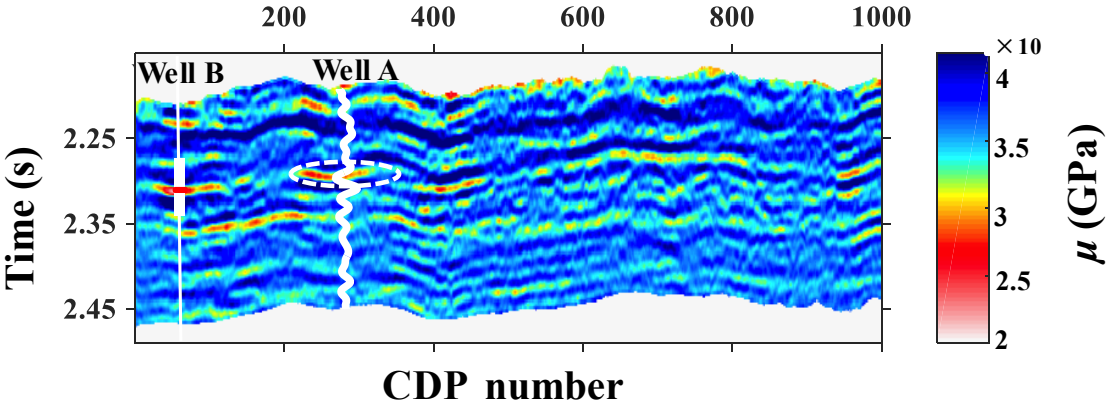

(b)

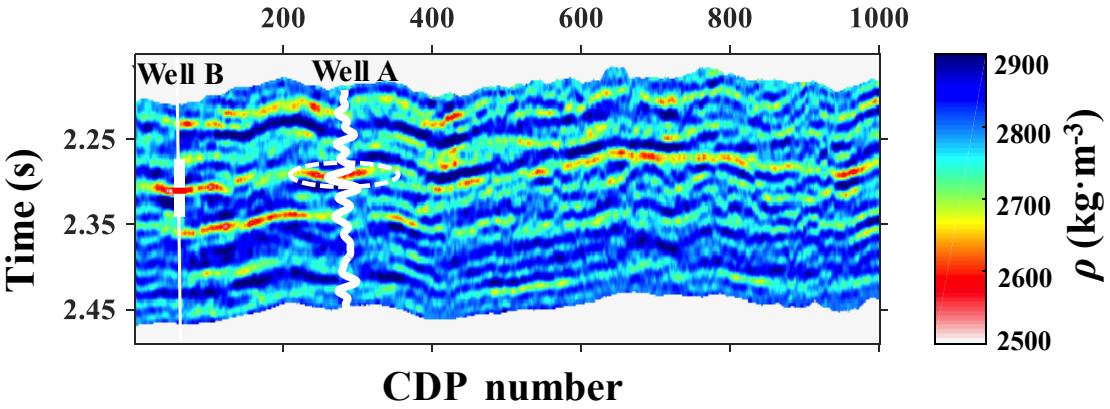

(c)

Fig. 10. Inverted results of fluid, rigidity, and density, where (a) the fluid term f, (b) the S-wave modulus μ, and (c) the density ρ.

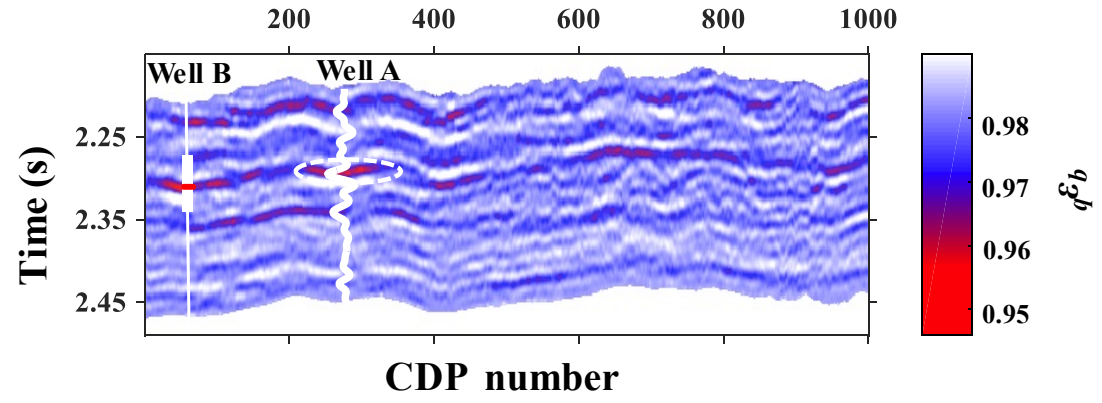

(a)

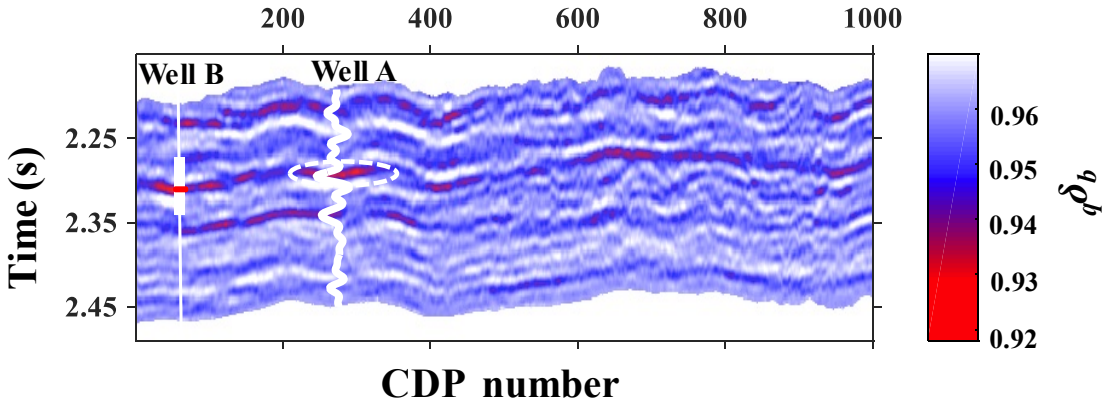

(b)

Fig. 11. Inverted Thomsen's anisotropy parameters, where (a) $_q\varepsilon_b$, and (b) $_q\delta_b$.

CONCLUSIONS

We demonstrate to discriminate the decoupled fluid term and fracture weaknesses in saturated transversely isotropic media with aligned fractures using the observable azimuthal data. First of all, we derive the fluid-saturated linearized weak-anisotropy approximations of stiffnesses with orthorhombic symmetry. Next a linearized PP-wave reflection coefficient is derived in orthorhombic anisotropic media. Finally, a Bayesian AEI inversion approach is proposed and applied to the synthetic and real data sets acquired in a saturated fractured porous reservoir with orthorhombic symmetry, Sichuan Basin, Southwest China. It turns out that the proposed method appears to generate reliable fluid term and fracture weaknesses for fluid discrimination and fracture characterization.

ACKNOWLEDGEMENTS

We acknowledge the sponsorship of National Natural Science Foundation of China (42004107).

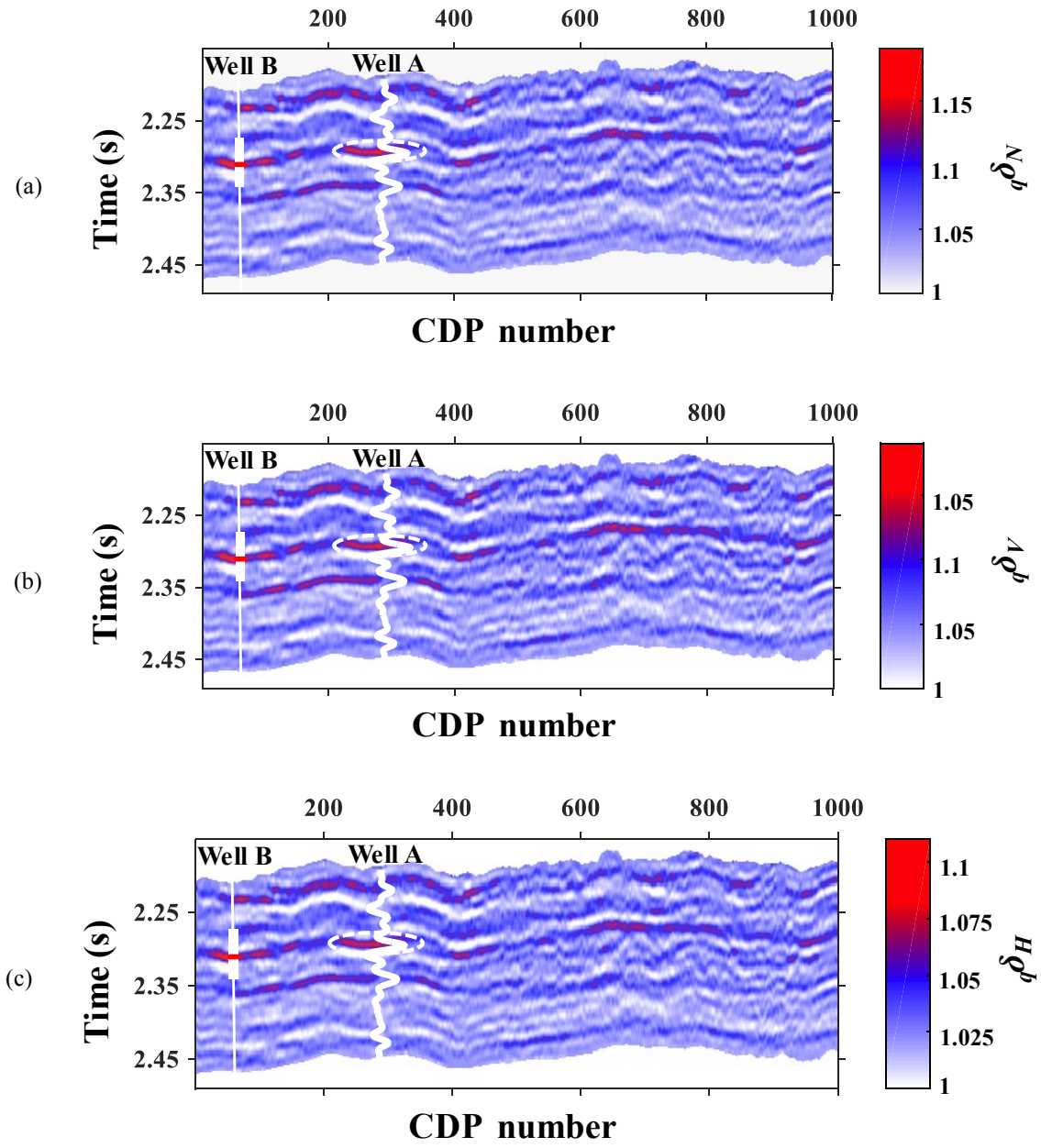

Fig. 12. Inverted results of fracture parameters, where (a) the normal fracture quasi-weakness $_q\delta_N$, (b) the vertical tangential fracture quasi-weakness $_q\delta_V$, and (c) the horizontal tangential fracture quasi-weakness $_q\delta_H$.

REFERENCES

Bachrach, R., Sengupta, M. and Salama, A., 2009. Reconstruction of the layer anisotropic elastic parameter and high resolution fracture characterization from P-wave data: a case study using seismic inversion and Bayesian rock physics parameter estimation. Geophys. Prosp., 57: 253-262.

Bachrach, R., 2015. Uncertainty and nonuniqueness in linearized AVAZ for orthorhombic media. The Leading Edge, 34: 1048-1056.

Bakulin, A., Grechka, V. and Tsvankin, I., 2000a. Estimation of fracture parameters from reflection seismic data-Part II: Fractured models with orthorhombic symmetry. Geophysics, 65: 1803-1817.

Bakulin, A., Grechka, V. and Tsvankin, I., 2000b. Estimation of fracture parameters from reflection seismic data-Part III: Fractured models with monoclinic symmetry. Geophysics, 65: 1818-1830.

Bakulin, A., Grechka, V. and Tsvankin, I., 2002. Seismic inversion for the parameters of two orthogonal fractures sets in a VTI background medium. Geophysics, 67: 292-299.

Chen, H., Pan, X., Ji, Y. and Zhang, G., 2017. Bayesian Markov Chain Monte Carlo inversion for weak anisotropy parameters and fracture weaknesses using azimuthal elastic impedance. Geophys. J. Internat., 210: 801-818.

Connolly, P., 1999. Elastic impedance. The Leading Edge, 18: 438-452.

Downton, J.E. and Roure, B., 2015. Interpreting azimuthal Fourier coefficients for anisotropic and fracture parameters. Interpretation, 3: ST9-ST27.

Far, M.E., Sayers, C.M., Thomsen, L., Han, D.H. and Castagna, J.P., 2013. Seismic characterization of naturally fractured reservoirs using amplitude versus offset and azimuth analysis. Geophys. Prosp., 61: 427-447.

Gassmann, F., 1951. Über die elastizität poröser Medien: Ver. Natur. Gesellsch. Zürich, 96: 1-23.

Golikov, P. and Stovas, A., 2010. New weak-contrast approximation for reflection coefficients in transversely isotropic media. J. Geophys. Engineer., 7: 343-350.

Gurevich, B., 2003. Elastic properties of saturated porous rocks with aligned fractures. J. Appl. Geophys., 54. 203-218.

Han, D.H. and Batzle, M.L., 2004. Gassmann's equation and fluid-saturation effects on seismic velocities. Geophysics, 69: 398-405.

Liu, E. and Martinez, A., 2012. Seismic Fracture Characterization. EAGE, Houten, Netherlands.

Martins, J.L., 2006. Elastic impedance in weakly anisotropic media. Geophysics, 71: 2092-2096.

Huang, L., Stewart, R.R., Sil, S. and Dyaur, N., 2015. Fluid substitution effects on seismic anisotropy. J. Geophys. Res., Solid Earth, 120: 850-863.

Ivanov, Y. and Stovas, A., 2017. Weak-anisotropy approximation for P-wave reflection coefficient at the boundary between two tilted transversely isotropic media. Geophys. Prosp., 65: 485-502.

Pan, X., Zhang, G., Chen, H. and Yin, X., 2017a. McMC-based nonlinear EIVAZ inversion driven by rock physics. J. Geophys. Engineer., 14: 368-379.

Pan, X., Zhang, G. and Yin, X., 2017b. Azimuthally anisotropic elastic impedance inversion for fluid indicator driven by rock physics. Geophysics, 82(6): C211-C227.

Pan, X., Zhang, G. and Yin, X., 2018a. Azimuthal seismic amplitude variation with offset and azimuth inversion in weakly anisotropic media with orthorhombic symmetry. Surv. Geophys., 39: 99-123.

Pan, X. and Zhang, G., 2018b. Model parameterization and PP-wave Amplitude Versus Angle and Azimuth (AVAZ) direct inversion for fracture quasi-weaknesses in weakly anisotropic elastic media. Survey. Geophys., 39: 937-964.

Pan, X., Zhang, G., Chen, H. and Yin, X., 2018c. Elastic impedance parameterization and inversion for fluid modulus and dry fracture quasi-weaknesses in a gas-saturated reservoir. J. Natur. Gas Sci. Engineer., 49: 194-212.

Pan, X. and Zhang, G., 2018d. Estimation of fluid indicator and dry fracture compliances using azimuthal seismic reflection data in a gas-saturated fractured reservoir. J. Petrol. Sci. Engineer., 167: 737-751.

Pšenčík, I. and Vavryčuk, V., 1998. Weak contrast PP wave R/T coefficients in weakly anisotropic elastic media. Pure Appl. Geophys., 151: 699-718.

Russel, B.H., Gray, D. and Hampson, D.P., 2011. Linearized AVO and poroelasticity. Geophysics, 76(3): C19-C29.

Sayers, C.M., 1994. P-wave propagation in weakly anisotropic media. Geophys. J. Internat., 116: 799-805.

Sayers, C., 1998. Misalignment of the orientation of fractures and the principal axes for P- and S-waves in rocks containing multiple non-orthogonal fracture sets. Geophys. J. Internat., 133: 459-466.

Sayers, C.M., 2009. Seismic characterization of reservoirs containing multiple fracture sets. Geophys. Prosp., 57: 187-192.

Schoenberg, M. and Protazio, J., 1990. 'Zoeppritz' rationalized and generalized to anisotropy. J. Acoust. Soc. Am., 88: S46.

Schoenberg, M. and Helbig, K., 1997. Orthorhombic media: Modeling elastic wave behavior in a vertically fractured earth. Geophysics, 62: 1954-1957.

Schoenberg, M. and Douma, J., 1998. Elastic wave propagation in media with parallel fractures and aligned cracks. Geophys. Prosp., 36: 571-590.

Shaw, R.K. and Sen, M.K., 2004. Born integral, stationary phase and linearized reflection coefficients in weak anisotropic media. Geophys. J. Internat., 158: 225-238.

Shaw, R.K. and Sen, M.K., 2006. Use of AVOA data to estimate fluid indicator in a vertically fractured medium. Geophysics, 71(3): C15-C24.

Thomsen, L., 1986. Weak elastic anisotropy. Geophysics, 51: 1954-1966.

Tsvankin, I., 1997. Anisotropic parameters and P-wave velocity for orthorhombic media. Geophysics, 62: 1292-1309.

Zong, Z. and Yin, X., 2016. Direct inversion of Young's and Poisson impedances for fluid discrimination. Geofluids, 16: 1006-1016.